Zero Knowledge Focusing in Millimeter-Wave Imaging Systems Using Gradient Approximation

Hojatollah Zamani, Mohammad Fakharzadeh, *Senior Member, IEEE*, Arash Amini, *Senior Member, IEEE*, Farokh Marvasti, *Life Senior Member, IEEE*

***Abstract*—This communication addresses the focusing problem in the millimeter-wave imaging systems. We categorize the focusing problem into the frequency focusing for wideband systems and the range focusing for narrow-band systems. In an out of focus wideband system, a shifted shadow of the object is present in the reconstruction, whereas for a range out of the focused system, the recovered images are blurred. To overcame these issues, first we theoretically show that the defocusing variations for both categories are bounded. Then, we present a universal formulation for focusing problem, which covers both wideband and the narrow-band systems. As the true focused images are sharp at the boundaries of the objects, our strategy for solving the problem is to maximize a defined sharpness metric. Moreover, we propose an autofocusing zero knowledge algorithm, which concerns with maximizing the sharpness metric from an unknown object, while the exact gradient of the cost function is unknown. The proposed method is suitable for practical applications, since it is simple, fast, and computationally efficient. The simulation results on synthetic and measured data are promising and support our claims that the proposed method increases the quality of the reconstruction.**

***Index Terms*—Millimeter wave imaging, range focusing, wideband focusing, coherent points, gradient approximation.**

I. Introduction

MILLIMETER-WAVE (MMW) imaging systems are widely used for different applications such as airport security, nondestructive tests, medical diagnosis and through wall imaging [1]–[3]. The MMW signals penetrate through thin dielectric layers, such as plastic, wood, and clothing, but reflect from metal and human body, which makes this band suitable for radar imaging in detecting flaws and concealed objects [4], [5].

In the case of wideband imaging, the TX sequentially sweeps all frequencies for each object pixel. Based on the geometric position of the TX and RX, the imaging system is categorized into the mono-static (same position for TX and RX) and multi-static (different positions for TX and RX). In this work, we consider the mono-static system for the sake of simplicity. Extending this work to the multi-static case is straightforward.

Most of the previous work in the image focusing problem are related to the synthetic aperture radar (SAR) imaging systems. In the context of focusing for MMW imaging systems, very few work exist. In [6] a multichannel autofocus technique based on a non-iterative algorithm is introduced, which finds the focused image in terms of basis functions formed with respect to the defocused image, relying on a condition on the image support to obtain a unique solution. In [7], an autofocus algorithm for wideband holographic imaging system is presented based on comparing the amplitude integral value of holographic imaging results. The algorithm reconstructs the image at different focusing distances and then selects the optimal focusing distance. A sparsity-driven technique for joint SAR imaging and phase error correction by using a non-quadratic regularization-based framework is introduced

*Authors are with the EE Department of Sharif University of Technology, Tehran, Iran (e-mail:hojatollah.zamani@ee.sharif.edu,{fakharzadeh, aamini, marvasti}@sharif.edu).

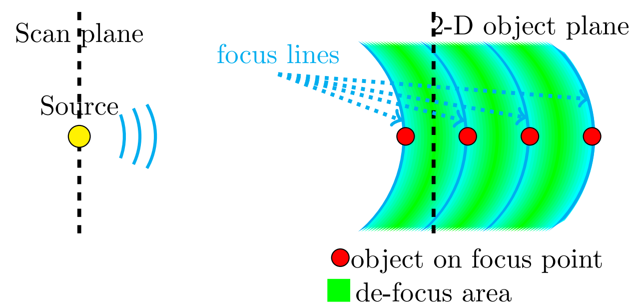

Fig. 1. Problem statement. The blue lines depict the focus points and the green color shows defocus area. To have a focused imaging setup, each of object point should placed in the red point.

in [8], where the phase errors are estimated and removed during image formation. The cost function in this work is composed of a data fidelity and a regularization term.

In [9], a method based on a holographic algorithm for near-field 3-D MMW imaging is proposed, where an extension of the single frequency autofocus holographic imaging algorithm for the wideband signals is studied. For SAR-based microwave imaging, a SVD-autofocus approach using range Doppler algorithm is introduced in [10]. A single-frequency autofocus millimeter wave holography scheme is developed in [11] in which the measured data is split into multiple sections and the autofocus algorithm is applied to each section. In [12], a software-hardware technique with the goal of quality improvement in the MMW imaging system is proposed, where the dual polarization arrays measure the co- and cross-polarization data with low cross-coupling.

To the best of our knowledge, there is no in-depth investigation of autofocus algorithms for MMW imaging systems. As shown in Fig. 1, the MMW wave propagates from a source point, where its intensity pattern is periodically repeated. If the object point is on the maximum intensity line (blue lines), which we call it *focus* point, the corresponding recovery is the sharpest (at the boundaries). We call the area between the blue lines as the defocused area, which means that the object is placed on a nonfocused point. In practice, some factors such as the range distance and sweeping frequencies cause the defocused measurements. Switching between frequencies is usually accompanied with the jitter; hence, the data is received with a different phase making it non-coherent. If the non-coherent data is directly used for reconstruction, the outcome will be a blurred image with considerable degradation of the quality. In this paper, first we determine the bound of defocusing variation theoretically for both single and wideband frequency systems. Then, we propose a gradient based approach to eliminate the defocus information by defining a sharpness metric. For a focused recovery, we apply concepts from the zero-knowledge beamforming [13]–[15]; the latter is concerned with maximizing the received power from a target with unknown Direction of Arrival, while the phase-voltage characteristics of the beamforming network is unknown. We use the same idea to estimate the unknown phases from an unknown object.

The rest of this paper is organized as follows. Section II describes the imaging system model. The main contributions are presented in Section III. The simulation and measurement results are presented in Section IV. Finally we conclude the paper in Section V.

II. System Model and Problem Setup

A. MMW Imaging System Model

The MMW mono-static imaging system can be mathematically modeled as follows. A pair of TX and RX antennas are located at the same place, which forms a transceiver. In a process of scanning an object plane (Fig. 2), the TX transmits the millimeter wave onto the object plane and the reflected signals from the illuminated object are captured by the RX. Assume that the transceiver antenna position, the corresponding illuminated point on the target, and the reflected wave are denoted by $(x', y', 0)$, (x, y, z_0) and $f(x, y)$, respectively. The scattered field at the receiver, is a linear combination of the reflected waves from all object points, which can be represented as [5]

$$s(x', y') = \iint f(x, y)\mathrm{e}^{-\mathrm{j}2kr}\mathrm{d}x\,\mathrm{d}y, \tag{1}$$

where $k = 2\pi/\lambda$ is the wavenumber, $s(x', y')$ is the measured signal by RX at position (x', y') and $r = \sqrt{(x - x')^2 + (y - y')^2 + z_0^2}$ is the Euclidean distance between the transceiver and the corresponding object point. A common approach of image recovery is the generalized synthesis aperture focusing technique (GSAFT) described in [5], which is summarized as

$$f(x, y) = \mathscr{F}^{-1}\{\mathscr{F}\{s(x', y')\}\mathrm{e}^{\mathrm{j}k_z z_0}\} \tag{2}$$

where $k_z = \sqrt{4k^2 - k_x^2 - k_y^2}$ and the operators $\mathscr{F}\{\cdot\}$ and $\mathscr{F}^{-1}\{\cdot\}$ represent the 2-D Fourier transform and its inverse, respectively. We use GSAFT as a benchmark method in our experiments for the purpose of comparison.

To model the imaging system in the discrete domain, let the matrices $\mathbf{S}_{\mathbf{M}\times\mathbf{N}}$ and $\mathbf{F}_{\mathbf{P}\times\mathbf{Q}}$ represent the measured data and the object plane, respectively. The discrete form of (1) is given by

$$\mathbf{S}[m, n] = \sum_{p=1}^{P}\sum_{q=1}^{Q}\mathbf{F}[p, q]\mathrm{e}^{-\mathrm{j}2kr[m,n,p,q]}, \tag{3}$$

where $r[m, n, p, q]$ is the Euclidean distance between the transceiver position $[m, n]$ (where m and n stand for the grid points on the x and y axes, respectively) and the object point $[p, q]$ ($r[m, n, p, q] = \sqrt{(m - p)^2 + (n - q)^2 + z_0^2}$). The wideband imaging model can be obtained by extending (3) to N_f frequencies $(f_i,\ i = 1, \cdots, N_f)$ as follows

$$\mathbf{S}[m, n, f_i] = \sum_{p=1}^{P}\sum_{q=1}^{Q}\mathbf{F}[p, q]\mathrm{e}^{-\mathrm{j}2\frac{2\pi}{c}f_i r[m,n,p,q]}. \tag{4}$$

B. Focusing Problem

Consider $\mathbf{S} \in \mathbb{C}^{M\times N\times N_f}$ to be the exactly focused measurements in the wideband system. In practice, $\mathbf{S}$ is corrupted by multiplicative phase errors which ultimately defocus the measurements. The phase error can be caused by either the range focusing problem related to the range/distance between the transceiver and the object planes, or the non-accurate frequency generation in the wideband imaging system. Mathematically, the defocused data can be represented as

$$\widehat{\mathbf{S}}[m, n, f_i] = \mathbf{S}[m, n, f_i]\mathrm{e}^{\mathrm{j}\varphi_e[m,n,f_i]}, \tag{5}$$

where $\varphi_e[m, n, f_i] \in [0, 2\pi]$ is the phase error related to the position $[m, n]$ and the frequency f_i. Using (4) and (5), a more realistic model is given by

$$\widehat{\mathbf{S}}[m, n, f_i] = \sum_{p=1}^{P}\sum_{q=1}^{Q}\mathbf{F}[p, q]\mathrm{e}^{-\mathrm{j}2\frac{2\pi}{c}f_i r[m,n,p,q]}\mathrm{e}^{\mathrm{j}\varphi_e[m,n,f_i]}. \tag{6}$$

The challenge is to recover a focused image $\mathbf{F}$ from the defocused measurements $\widehat{\mathbf{S}}$.

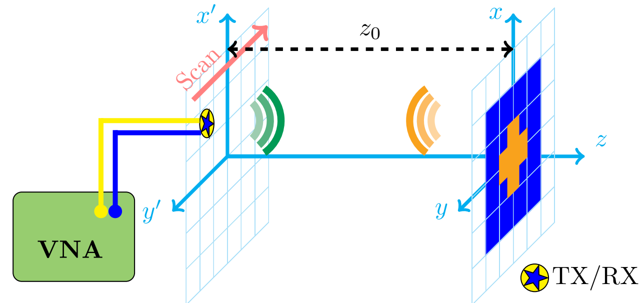

Fig. 2. Mono-static imaging system model. The TX antenna impinging EM wave toward the object and the reflected wave is measured by the RX antenna.

III. Main Results

In this section, we first explore the focusing problem and theoretically derive the bounds of defocusing variations for both categories (range and frequency focusing problem). Then, to compensate the defocusing effects, we propose an autofocusing algorithm based on gradient estimation, which maximizes a defined sharpness metric.

A. Single Frequency Focusing

Consider the single frequency imaging system. Let the system operate within the focus range of z_1 (distance between transceivers and object planes). According to (3) and the wave propagation property, the defocus distance z_0 with an additional phase φ can generate the coherent data. By assuming $a = \sqrt{(m - p)^2 + (n - q)^2}$, the following equations should be satisfied

$$\mathrm{e}^{-2\mathrm{j}\frac{2\pi}{\lambda}\sqrt{a^2+z_0^2}} = \mathrm{e}^{-2\mathrm{j}\frac{2\pi}{\lambda}\sqrt{a^2+z_1^2}}\mathrm{e}^{-\mathrm{j}\varphi} \tag{7}$$

$$\tfrac{4\pi}{\lambda}\sqrt{a^2 + z_0^2} = \tfrac{4\pi}{\lambda}\sqrt{a^2 + z_1^2} + \varphi \tag{8}$$

$$z_0 = \sqrt{(\sqrt{a^2 + z_1^2} + \tfrac{\lambda}{4\pi}\varphi)^2 - a^2}. \tag{9}$$

By inserting the minimum and the maximum values of φ, the defocus range is determined as

$$z_1 \leq z_0 \leq \sqrt{(\sqrt{a^2 + z_1^2} + \tfrac{\lambda}{2})^2 - a^2}, \tag{10}$$

For the middle point where $a = 0$, the minimum defocus range ($z_1 \leq z_0 \leq z_1 + \frac{\lambda}{2}$) is achieved. It is observed that, the defocusing distance is bounded by an affine function of the wavelength. To better illustrate this point, the next focus distance (upper bound of

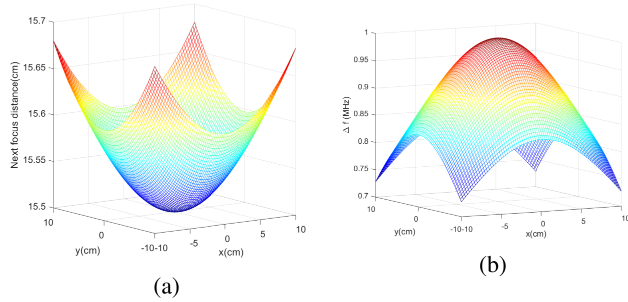

Fig. 3. (a) Focus distance for $f = 30$ GHz and area $[-10\text{cm} \times 10\text{cm}]$. (b) Δf for $z = 15$ cm and area of $[-10\text{cm} \times 10\text{cm}]$.

(10)) is depicted for all grid points in Fig. 3(a) for the operating frequency of 30 GHz. Besides, the scanning area is $10\text{cm} \times 10\text{cm}$ covering the whole object and the original focusing distance is $z_1 = 15$ cm. This bound indicates that the amount of blur on the reconstruction is limited. To achieve a high quality in reconstruction, an accurate estimation of the range is required. Due to the physical limitations of the system, this is an important concern in practice. In fact, the system requires a mechanism to control this effect automatically. Here, we shall control this by introducing an autofocusing algorithm.

B. Wideband focusing

An important issue that appears in wideband imaging systems is the effect of frequency perturbation, which impacts the overall quality of image reconstruction. In a wideband imaging system that scans a 2-D object, due to the periodicity of wave propagation, increasing the frequency band beyond a threshold is redundant, as coherent data will be repeated. Here, our goal is to theoretically determine the interval between two consecutive focus frequencies based on imaging model; this limits the perturbation range. In fact, we investigate the extent to which the measured data is varied by sweeping the wave frequency. With the same approach as the range focusing analysis, the measured data associated with frequency f_1 can be regenerated by another frequency f_2 with additional phase φ. Therefore, we get

$$\mathrm{e}^{-\mathrm{j}2\frac{2\pi}{c}f_2\sqrt{a^2+z^2}} = \mathrm{e}^{-\mathrm{j}2\frac{2\pi}{c}f_1\sqrt{a^2+z^2}}\mathrm{e}^{-\mathrm{j}\varphi} \tag{11}$$

$$\tfrac{4\pi}{c}f_2\sqrt{a^2+z^2} = \tfrac{4\pi}{c}f_1\sqrt{a^2+z^2} + \varphi \tag{12}$$

$$f_2\sqrt{a^2+z^2} = f_1\sqrt{a^2+z^2} + \tfrac{c}{4\pi}\varphi \tag{13}$$

$$f_2 = f_1 + \tfrac{c}{4\pi\sqrt{a^2+z^2}}\varphi \tag{14}$$

Now, by checking the extreme values of φ, we determine the frequency range as

$$f_1 \leq f_2 \leq f_1 + \frac{c}{2\sqrt{a^2+z^2}} \tag{15}$$

Interestingly, for the case of middle point ($a = 0$), we get the maximum range $0 \leq \Delta f \leq \frac{c}{2z}$ where $\Delta f = f_2 - f_1$. Therefore, as mentioned earlier, the range of effective wave frequencies for imaging is limited and the captured data will be periodically repeated by increasing the frequency value. For instance, if $z = 15\text{cm}$, then, $0 \leq \Delta f \leq 1\text{MHz}$. Further, the range of Δf depends on the value of a, (Fig. 3(b) shows Δf range for $z = 15\text{cm}$ and scan area of $[-10\text{cm} \times 10\text{cm}]$).

C. Sharpness metric

We express the autofocus issue as an optimization problem, where the objective is to maximize the received power from a desired object. The only information about the data is that the measured signal at each frequency is corrupted by a phase error. By observing $\widehat{\mathbf{S}}[m, n, f_i]$ in (6), it is not possible to uniquely extract mathematical expressions for both $\mathbf{F}$ and $\boldsymbol{\varphi}_e$. However, if $\boldsymbol{\varphi}_e$ is known, $\mathbf{F}$ can be derived from $\widehat{\mathbf{S}}[m, n, f_i]$ by an inverse Fourier transform. We define each point of the output focused image with phase vector $\boldsymbol{\varphi}_{pq} = [\varphi_1, \varphi_2, \cdots, \varphi_{N_f}]$ as follows

$$h_{pq}(\varphi_1, \varphi_2, \cdots, \varphi_{N_f}) = \sum_{i=1}^{N_f}\sum_{m=1}^{M}\sum_{n=1}^{N}\widehat{\mathbf{S}}[m, n, f_i]\mathrm{e}^{\mathrm{j}\varphi[p,q,i]}\mathrm{e}^{\mathrm{j}2k[i]r[m,n,p,q]}. \tag{16}$$

The algorithm requires a metric to estimate the phases. Because of the point-wise nature of MMW imaging model, image sharpness is a proper indicator of the amount of focus. The aim of the proposed algorithm is to determine the phase values in the search space that maximize a sharpness metric; this metric is formed by individual pixel contributions. More specifically, we define the metric $H(\boldsymbol{\varphi}) = \sum_p\sum_q |h_{pq}(\boldsymbol{\varphi}_{pq})|^2$ by taking the intensity of each pixel $h_{pq}(\boldsymbol{\varphi}_{pq})$ into account in form of:

$$\underset{\boldsymbol{\varphi}}{\operatorname{argmax}}\ H(\boldsymbol{\varphi}). \tag{17}$$

D. Proposed Algorithm

We propose an iterative gradient method to estimate the phases. Lets $\boldsymbol{\varphi}(n) = [\varphi_1(n), \varphi_2(n), \cdots, \varphi_N(n)]$ denote the estimated phases of $N = P \times Q \times N_f$ points at iteration n. Using the gradient estimation method, the new phase vector $\boldsymbol{\varphi}(n+1)$ is updated according to

$$\boldsymbol{\varphi}(n+1) = \boldsymbol{\varphi}(n) + 2\mu\nabla_{\boldsymbol{\varphi}}H(n) \tag{18}$$

where μ is the step-size parameter of the algorithm, and $\nabla_{\boldsymbol{\varphi}}H(n)$ denotes the gradient of the metric with respect to $\boldsymbol{\varphi}$. Since the exact evaluation of $\nabla_{\boldsymbol{\varphi}}H(n)$ is difficult, we replace it with an approximate vector, such as [14]

$$\nabla_{\boldsymbol{\varphi}}H(n) \approx [\hat{g}_1(n), \hat{g}_2(n), \cdots, \hat{g}_N(n)] \tag{19}$$

where each component $\hat{g}_k(n)$ is the approximate partial derivative of $H(n)$ w.r.t. $\varphi_k(n)$. To estimate the gradient of a multi-variable function, the sequential two-side approximation method is used. In this approach, two perturbations with opposite signs are applied to determine the centered finite-difference approximation of each gradient component

$$\hat{g}_k(n) = \frac{H(\cdots, \varphi_k(n)+\delta, \cdots) - H(\cdots, \varphi_k(n)-\delta, \cdots)}{2\delta}. \tag{20}$$

We further update μ automatically for fast convergence of the algorithm. Throughout the iterations, as the estimations approach the maximizer of the metric, we need to decrease the step-size μ to control the ripples. For this goal, we update μ as $\mu_n = \mu_0\mathrm{e}^{-\mathrm{kn}}$ (where k is a decay factor) in an iteration whenever the sum of the object points of the image is increased. As we do not know the exact boundary of the true object points, we roughly estimate it by applying a fast and simple inverse propagation technique and select the points with intensities larger than 90% of the maximum value.

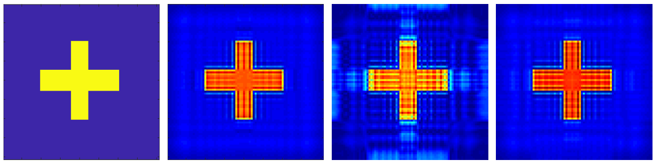

(a) (b) (c) (d)

Fig. 4. Recovery of a cross shape: (a) the original shape, (b) perfectly focused recovery, (c) nonfocused recovery with SSIM= 0.4419, (d) auto-focused recovery using the proposed algorithm with SSIM = 0.9371

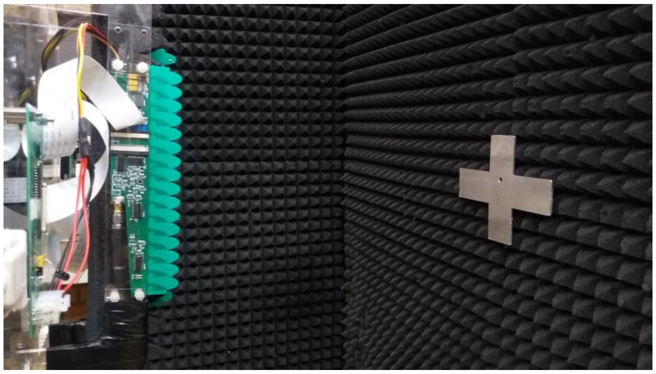

Fig. 5. The practical imaging system setup. The transceiver moves along the scan plane and measures the reflected waves from the object.

IV. Simulation and measurement results

In this section, we evaluate the proposed autofocusing method. Different scenarios including synthetic and measured data with variety of shapes are considered. The parameter δ of the proposed algorithm is set to 10^{-4}. We evaluate the image reconstruction quality by the structural similarity index measure (SSIM) metric [16].

In the first scenario, the distance between the transceiver and object planes is set as $30\mathrm{cm}$, and the discretized object plane has 20×58 points (Fig. 2). The synthetic object is shown in Fig. 4(a). The reconstructed shape using the GSAFT algorithm is depicted in Fig. 4(b). We now add a random phase noise to the data and directly recover it as shown in Fig. 4(c), where the SSIM is 0.4419. By applying the proposed algorithm, the phase noise is compensated in Fig. 4(d) and the SSIM is increased to 0.9371.

For the rest of the experiments, we evaluate the proposed method on a practical imaging system, which is depicted in Fig. 5. The imaging system consists of two horn antennas with $20\mathrm{dB}$ gain at Ka-band ($26\mathrm{GHz}$-$40\mathrm{GHz}$) used as TX and RX antennas, an RF amplifier with $18\mathrm{dB}$ gain and a mechanical scanning system, which moves the antennas for scanning the object in Cartesian plane. The TX and RX antennas are connected to a HP8722ES network analyzer, which transmits and receives millimeter-wave signals. The whole system is placed inside an anechoic chamber, where undesired reflections are absorbed.

For the second scenario, we use the measured data of an aluminium cross with the same settings as in the first scenario. A sample of the recorded data is shown in Fig. 6(a). The recovered images based on the nonfocused and autofocused data are depicted in Figs. 6(a2) and 6(a3), respectively. The results indicate that the proposed algorithm focuses the data successfully and the recovered shape boundary is sharp.

For the next experiments, we measure the data of an "F" shape metal object and a real knife in different imaging settings. Here, the objects are placed 16 cm away from the receiver. For scanning the "F" shape object, the wave frequency is swept from $28.5\mathrm{GHz}$ to $31\mathrm{GHz}$ with the step of $6.25\mathrm{MHz}$. Also, the dimensions of the measured data is 50×50 points. In the case of the real knife, the scanned area is 93×104 points and the system operates at 11 different frequencies within the range of $26\mathrm{GHz}$ to $35\mathrm{GHz}$ with the step of $900\mathrm{MHz}$. Here, the object-transceiver distance is set to 45 cm. The results of these experiments are also depicted in Fig. 6. The results confirm the success of the proposed autofocusing method, which compensates the phase noise and increases the reconstruction quality. To show the convergence of the proposed algorithm, we randomly select 200 points of the measured data of the "F" shape and draw the estimated phases per iteration in Fig. 7. It is observed that after 8 iterations, the estimated phases almost match those used for generating Fig. 6(c3).

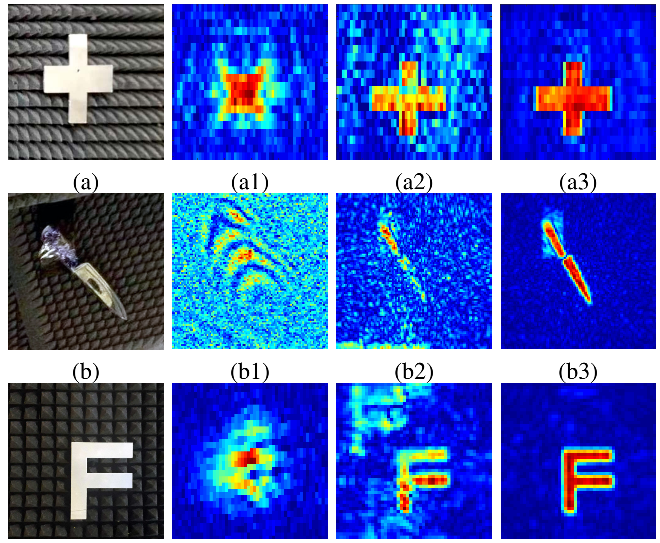

(a) (a1) (a2) (a3)
(b) (b1) (b2) (b3)
(c) (c1) (c2) (c3)

Fig. 6. Recovery of a "cross", the shape "F", and a "knife" from the real measurements. (a), (b), and (c) are the optical images. (a1), (b1), and (c1) display the samples of the measured data. (a2), (b2), and (c2) are the recovered images using GSAFT based on nonfocused data. (a3), (b3), and (c3) show the recovered images using the proposed autofocusing algorithm.

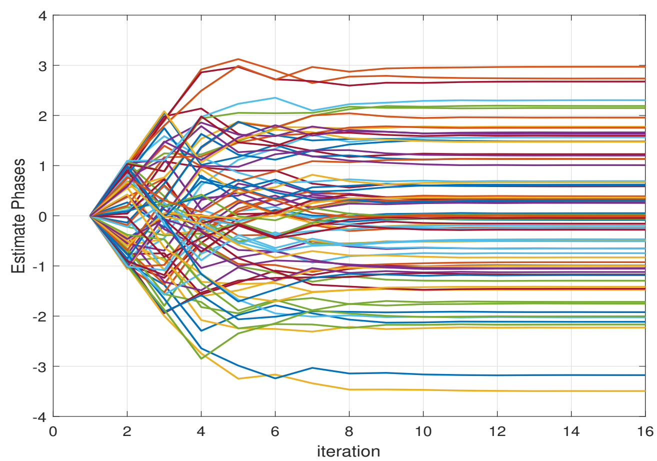

Fig. 7. Defocused phase estimation curve versus iteration for 200 points of measured data using proposed algorithm.

We evaluate the execution time of the proposed algorithm for an image size of 55×55 pixels and 201 different frequencies. On average, the phase estimation per point takes 2.8 microsecond. Overall, the algorithm takes 14.33 s to converge at all the points within 40 iterations. This evaluation is implemented in MATLAB 2019b on a workstation with Intel(R) Core(TM) i7 $-$ 4930K CPU @3.40GHz (12 CPUs) and 16GB RAM.

V. Conclusion

In this paper, the problem of 2-D image recovery in wideband imaging systems is addressed. We showed that based on periodicity of the phase term in wideband imaging, the measured data points are repeated at different frequencies and the bound of frequency variations is extracted. By combining the data on the coherent points, a significant improvement in the image reconstruction was observed. Moreover, we proposed a practical autofocusing algorithm based on the defined sharpness metric to determine and compensate for the phase perturbation at different frequencies. The proposed algorithm was applied to both synthetic and measured data to evaluate its performance. The quality of the image recovery was improved and our algorithm outperformed the state-of-the-art algorithms.

References

[1] V. M. Patel, J. N. Mait, D. W. Prather, and A. S. Hedden, "Computational millimeter wave imaging: Problems, progress, and prospects," *IEEE Signal Processing Magazine*, vol. 33, no. 5, pp. 109–118, 2016.

[2] A. Elboushi and A. Sebak, "MMW Sensor for Hidden Targets Detection and Warning Based on Reflection/Scattering Approach," *IEEE Trans. Antennas Propag.*, vol. 62, no. 9, pp. 4890–4894, 2014.

[3] H. Zamani and M. Fakharzadeh, "1.5-d sparse array for millimeter-wave imaging based on compressive sensing techniques," *IEEE Transactions on Antennas and Propagation*, vol. 66, no. 4, pp. 2008–2015, April 2018.

[4] M. C. Kemp, "Millimetre wave and terahertz technology for detection of concealed threats - a review," in *15th Int. Conf.Terahertz Electronics*, Sept 2007, pp. 647–648.

[5] D. M. Sheen, D. L. McMakin, and T. E. Hall, "Three-dimensional millimeter-wave imaging for concealed weapon detection," *IEEE Trans. Microw. Theory Tech.*, vol. 49, no. 9, pp. 1581–1592, 2001.

[6] R. L. Morrison, M. N. Do, and D. C. Munson, "Mca: A multichannel approach to sar autofocus," *IEEE transactions on image processing*, vol. 18, no. 4, pp. 840–853, 2009.

[7] H. Cheng, S. Li, H. Zheng, H. Jing, and H. Sun, "A w-band auto-focus holographic imaging system for security screening," *IEICE Electronic Express*, vol. 14, no. 11, p. 20170347, 2017.

[8] N. O. Onhon and M. Cetin, "A sparsity-driven approach for joint sar imaging and phase error correction," *IEEE Transactions on Image Processing*, vol. 21, no. 4, pp. 2075–2088, 2012.

[9] S. Li, G. Zhao, H. Sun, and M. Amin, "Compressive sensing imaging of 3-d object by a holographic algorithm," *IEEE Transactions on Antennas and Propagation*, vol. 66, no. 12, pp. 7295–7304, 2018.

[10] M. D. Buhari, G. Y. Tian, and R. Tiwari, "Microwave-based sar technique for pipeline inspection using autofocus range-doppler algorithm," *IEEE Sensors Journal*, vol. 19, no. 5, pp. 1777–1787, 2019.

[11] H. Cheng, J. Gu, Y. Cheng, S. Li, and H. Sun, "Multi-section autofocus millimeter-wave holography," in *2016 IEEE MTT-S International Microwave Symposium (IMS)*, 2016, pp. 1–3.

[12] M. Rezaei, H. Zamani, M. Fakharzadeh, and M. Memarian, "Quality improvement of millimeter-wave imaging systems using optimized dual polarized arrays," *IEEE Transactions on Antennas and Propagation*, pp. 1–1, 2021.

[13] M. Fakharzadeh, S. Safavi-Naeini, S. H. Jamali, and P. Mousavi, "Zero-knowledge beamforming of phased array antennas based on simultaneous perturbation gradient approximation," in *2006 IEEE Antennas and Propagation Society International Symposium*, 2006, pp. 537–540.

[14] P. Mousavi, M. Fakharzadeh, S. H. Jamali, K. Narimani, M. Hossu, H. Bolandhemmat, G. Rafi, and S. Safavi-Naeini, "A low-cost ultra low profile phased array system for mobile satellite reception using zero-knowledge beamforming algorithm," *IEEE Transactions on Antennas and Propagation*, vol. 56, no. 12, pp. 3667–3679, 2008.

[15] M. Fakharzadeh, S. H. Jamali, P. Mousavi, and S. Safavi-Naeini, "Fast beamforming for mobile satellite receiver phased arrays: Theory and experiment," *IEEE Transactions on Antennas and Propagation*, vol. 57, no. 6, pp. 1645–1654, 2009.

[16] Zhou Wang *et al.*, "Image quality assessment: from error visibility to structural similarity," *IEEE Transactions on Image Processing*, vol. 13, no. 4, pp. 600–612, April 2004.